www.sciencemag.org/content/359/6376/666/suppl/DC1

Supplementary Materials for

A topological quantum optics interface

Sabyasachi Barik, Aziz Karasahin, Christopher Flower, Tao Cai, Hirokazu Miyake, Wade DeGottardi, Mohammad Hafezi,* Edo Waks*

*Corresponding author. Email: hafezi@umd.edu (M.H.); edowaks@umd.edu (E.W.)

Published 9 February 2018, *Science* **359**, 666 (2018)
DOI: 10.1126/science.aaq0327

This PDF file includes:

Materials and Methods

Device Fabrication

To fabricate the device, we began with an initial wafer composed of a 160 nm GaAs membrane on top of 1 μm sacrificial layer of Al0.8Ga0.2As with quantum dots grown at the center. The quantum dot density was approximately 50 μm-2. Based on the given quantum density and cross-sectional area of the waveguide, the probability of finding two dots in the structure with the same resonance is less than 0.7%. Thus, it is extremely unlikely in a given device for a photon emitted by one dot to be scattered by a second.

We fabricated the topological photonic crystal structure using electron beam lithography, followed by dry etching and selective wet etching of the sacrificial layer. We first spin-coated the wafer with ZEP520A e-beam resist, then patterned the structure using 100 keV acceleration voltage and developed the resist using ZED50 developer. After patterning, we used chlorine-based inductively coupled plasma etching to transfer the pattern on the GaAs membrane. We finally performed selective wet etching using HF to create a suspended structure with air on top and bottom. The rectangular structures in the periphery are included to facilitate undercut of the sacrificial layer.

Sharp corners with straight side walls are essential to observe the topological helical edge modes. It is confirmed via simulation that triangles with rounded corners are detrimental for the device operation. However, even with highly directional dry etch, creating sharp features like triangles is challenging at such small length scales. We observed – by using a regular mask design (as shown in Figure S1.A) – that etching causes widening of holes which eventually results in rounded corners much like a Reuleaux triangle (Figure S1.B). We used a modified mask design to overcome this challenge. Triangles with shrunk edges shown in Figure S1.C are used as a mask; this results in sharp triangles with edge lengths of 140 nm. Close up SEM image of final structure is shown in Figure S1.D.

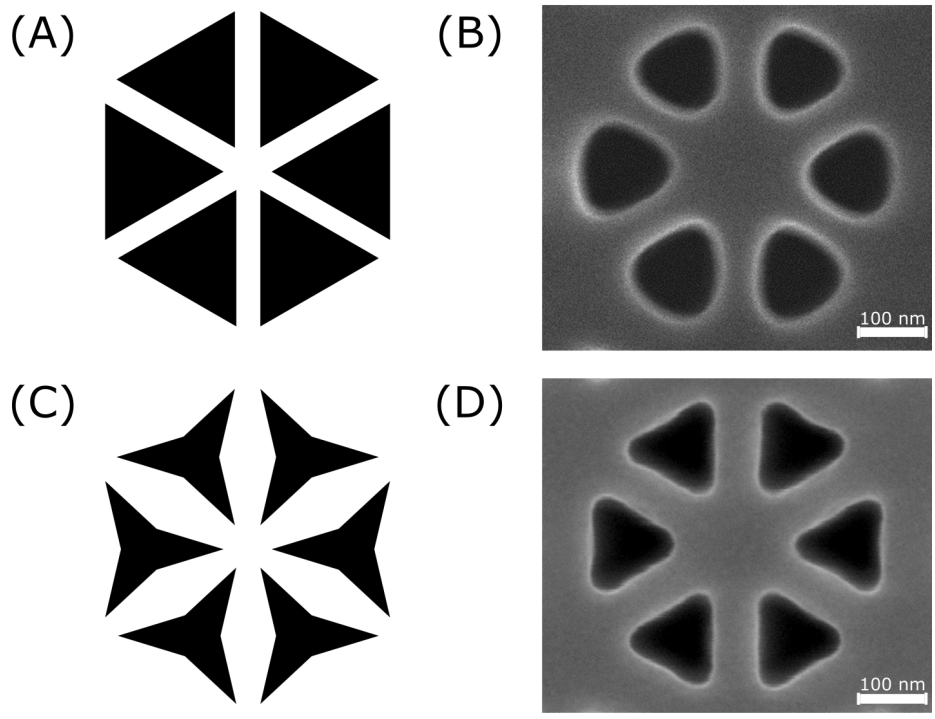

Figure S1. Mask design for fabrication of triangles. (**A**) Layout of regular mask. (**B**) SEM image of rounded triangles resulted from use of regular mask. (**C**) Layout of modified mask; triangles are bent from edges to mitigate etching imperfections. (**D**) SEM image of sharp triangles fabricated with use of modified mask.

Experimental Setup

To perform measurements, we mounted the sample in a closed-cycle cryostat and cooled it down to 3.6 K. A superconducting magnet, contained within the closed-cycle refrigerator, surrounds the sample and applies a magnetic field of up to 9.2 T along the out-of-plane (Faraday) direction in order to generate a Zeeman splitting between the two bright excitons of the quantum dot. We performed all sample excitation and collection using a confocal microscope with an objective lens with numerical aperture of 0.8. We collected the emission and focused it onto a single mode fiber to perform spatial filtering. To perform spectral measurements, we injected the signal to a grating spectrometer with a spectral resolution of 7 GHz. For autocorrelation measurements, we used a flip mirror to couple the light out of the spectrometer and processed the filtered emission using Hanbury-Brown Twiss intensity interferometer composed of a 50/50 beamsplitter, two Single Photon Counting Modules (SPCMs) and a PicoHarp 300 time correlated single photon counting system.

The quantum dots are less than 20 nm in diameter, while the laser spot size is approximately 0.4 um. The density of quantum dots are 50 μm^{-2}, which means that there are approximately 25 dots within the excitation spots. However, due to the large

inhomogeneous broadening of the ensemble, each of these dots emits at a different wavelength. We isolate individual quantum dots by spectral filtering using a grating spectrometer with a resolution of 0.02 nm. The spectrometer selects the emission from only a single dot, as evidenced by the anti-bunching dip observed in Fig. 4D-E which dips below 0.5.

Supplementary Text

Device Design

Figure S2 shows a schematic of the device design. We begin with a honeycomb lattice of equilateral triangles exhibiting hexagonal symmetry as our baseline structure. This lattice is a triangular lattice of cells consisting of six equilateral triangular holes, indicated by the dashed line. We use a lattice constant of a_0 = 445 nm, an edge length of the equilateral triangle of s=140 nm, and a slab thickness of h = 160 nm. R defines the distance from the center of a cell to the centroid of a triangle. In this structure a perfect honeycomb lattice corresponds to $R = a_0/3$.

With these parameters we obtain doubly degenerate Dirac cones at 319 THz (940 nm). We form the two mirrors by concentrically expanding or contracting the unit cell.

We create topologically distinct regions by deforming the unit cell of the pristine honeycomb lattice. In the blue region in Figure 1A, we concentrically shift the triangular holes by increasing R to $1.05a_0/3$, thereby shifting all the triangular holes in an individual cell outward. This deformation results in the band structure shown in Figure 1C. In the yellow region, we decrease R to $0.94a_0/3$, which pulls the holes towards the center resulting in the band structure shown in Figure 1D.

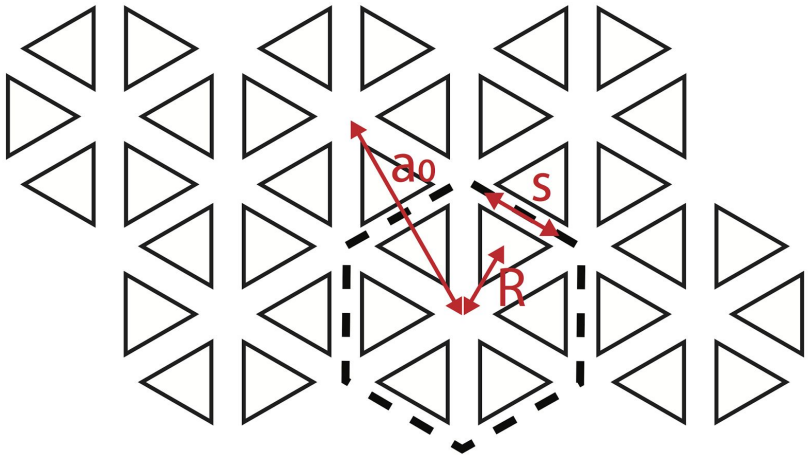

Figure S2. Design of honeycomb-like photonic crystal.

Symmetry-Protected Topological Photonic Crystal

Once thought to be limited to the quantum Hall effect, the notion of topological insulating phases has revolutionized condensed matter physics and is the inspiration for topological photonic systems. These states are based on the fact that insulating Hamiltonians which obey certain combinations of symmetries (such as time-reversal) can be classified according to their topology. The photonic crystal considered here is described by a Z_2 topological invariant, which takes the value 0 (trivial phase) or 1 (topological phase). The physical manifestation of this is that between regions of differing topology, protected edge modes are found. These modes cannot be coupled since such a term would violate the protected symmetry.

The photonic crystal considered in this work is an analog of a quantum spin Hall system for photons and is discussed in greater detail in *(20, 21)*. The quantum spin Hall system exhibits topological protection that is based on time-reversal symmetry. In the context of the photonic crystal, the role of time-reversal symmetry is played by the six-fold rotational (C_{6v}) crystal symmetry of the hexagonal unit cell. In the energy range of interest, the band structure of the system is described by the Dirac equation, where the mass is controlled by the spacing of triangles in a hexagonal cluster. The topological Z_2 index reflects the sign of the mass, and is positive (negative) for compressed (expanded) regions. The topologically protected counterpropagating modes exist in the region at which the mass changes sign. In the context of the Dirac equation, these states are known as Jackiw-Rebbi states *(21)*.

The yellow and blue regions in Figure 1A represent the topologically distinct phases discussed above. Topological modes exist at the boundary, and are protected from any disorder which respects the six-fold crystal symmetry. Disorder that breaks this symmetry can lead to the backscattering of the edge modes. In fact, the formation of the interface itself can break this symmetry, albeit weakly. Through extensive simulations, we have found that the zig-zag interface in our device adequately preserves the crystalline symmetry, thereby minimizing the coupling between the counterpropagating edge modes. Figure S3.A shows the propagating mode for this interface, while Figure S3.B shows the propagation length of the waveguide as a function of wavelength. The simulated propagation length is approximately 22 μm. We note that although this propagation length is longer than our device (15 μm), it is short compared to a conventional photonic crystal waveguide. This reduced propagation length is due to the fact that we are forming a guided mode from a perturbed hexagonal lattice. In the pure hexagonal lattice all modes exist below the light line (21), but after perturbation the structure exhibits a triangular rather than hexagonal symmetry. This change in symmetry can cause modes to scatter to the **Γ** point which is above the light line. Using a progressively weaker perturbation leads to less scattering, and therefore longer propagation lengths (Figure S3.C), which must be traded off with a narrower topological bandgap. In Figure S3.D, we show simulations illustrating the robustness of the edge modes to a certain type of defect. The defect, an entire missing cell, breaks C_{6v} crystal

symmetry. However, this defect does not adversely affect the transmission in the gapped region. We should note that the disorder seen in our device is considerably less severe.

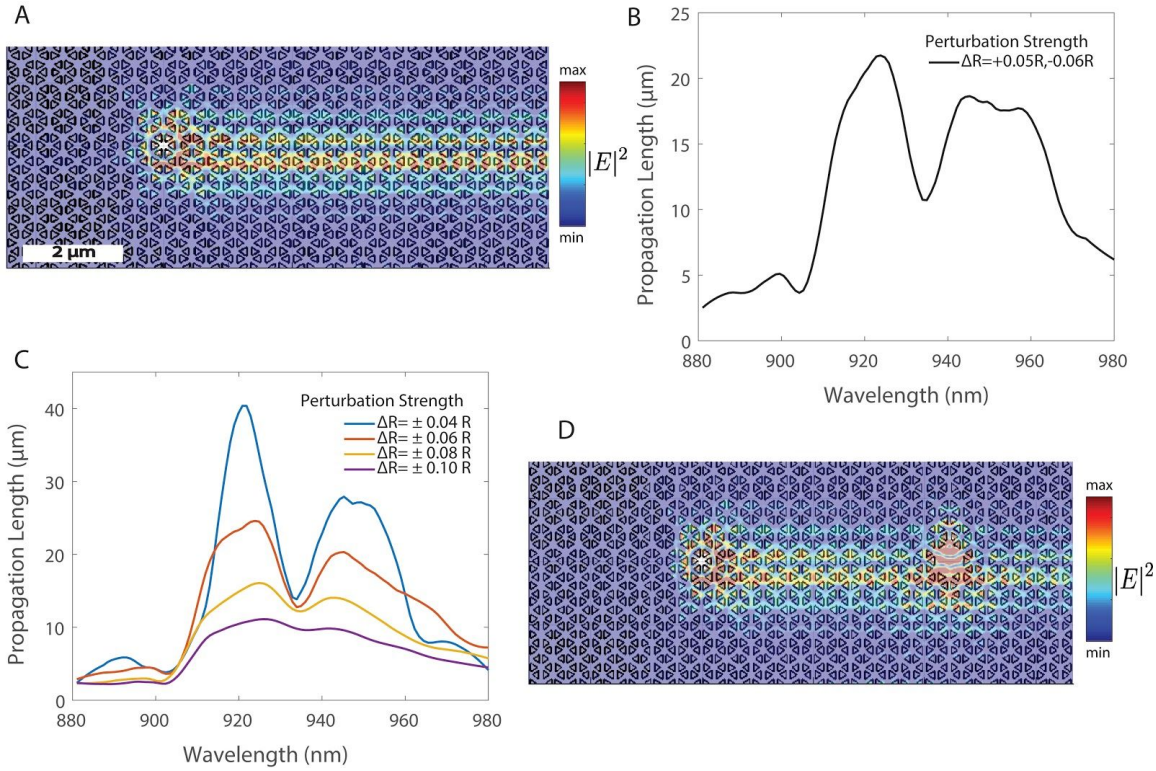

Figure S3. Propagation loss and robustness of edge modes. (A) Simulation showing electric field intensity for propagation of edge state in a topological waveguide without a defect **(B)** Propagation length for the edge state in our measured device. The perturbation parameter is $\Delta R = R_0 - R_{in/out}$, where R is defined as in Fig S2. The parameter R_0 corresponds to the unperturbed original honeycomb lattice, and $R_{in/out}$ characterize the inward/outward perturbed lattices, respectively. **(C)** Simulation results showing propagation lengths of edge states in the topological photonic crystal waveguide as we change ΔR. **(D)** Simulation showing electric field intensity of edge states as it propagates around a defect.

Grating Calibration

Since both left and right grating couplers are fabricated under similar condition they are identical in terms of coupling efficiency. To test this fact we calibrated them with respect to. the transmission spectrum of the topological waveguide. Figure S4.A shows the different positions on the device. We shine an intense excitation beam of 780 nm with 1.5uW power at the center of the waveguide (M). At this high power all the quantum dots are saturated and emit a broadband spectrum ranging from 900-980nm. We collected the transmitted signal from left (L) and right grating (R). Figure S4.B shows almost equal counts coming from both the gratings with almost overlapping transmission spectrum. Additionally, the area under the curves give approximately 40 million counts/sec for the gratings thus indicating equal coupling efficiency.

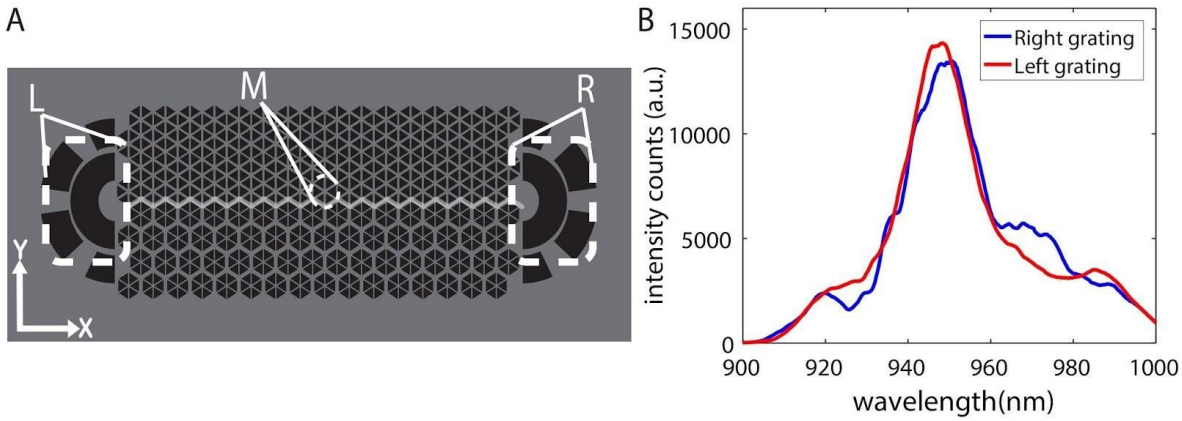

Figure S4. Transmission data from left and right gratings. (**A**) Scheme for excitation and collection. (**B**) Transmitted signal collected from two gratings.

Polarization of Quantum Dots in Bulk Under Magnetic Field

We first measured the photoluminescence from a bare QD in the bulk. With the application of magnetic field QD emission spectrum splitted into two branches with circularly polarized emission as shown in Figure S5. A and denoted by $\sigma^{\pm}$. At a very high magnetic field of 3T the separation between two branches becomes 0.3nm. at this stage to verify the selection rules we introduced a quarter wave plate and a polarizer before collecting the signal. Figure S5.B shows recorded photoluminescence obtained by rotating the polarizer angle. The antiphase relation between the two branches along with the detection scheme confirms that they are indeed circularly polarized in bulk under high magnetic field.

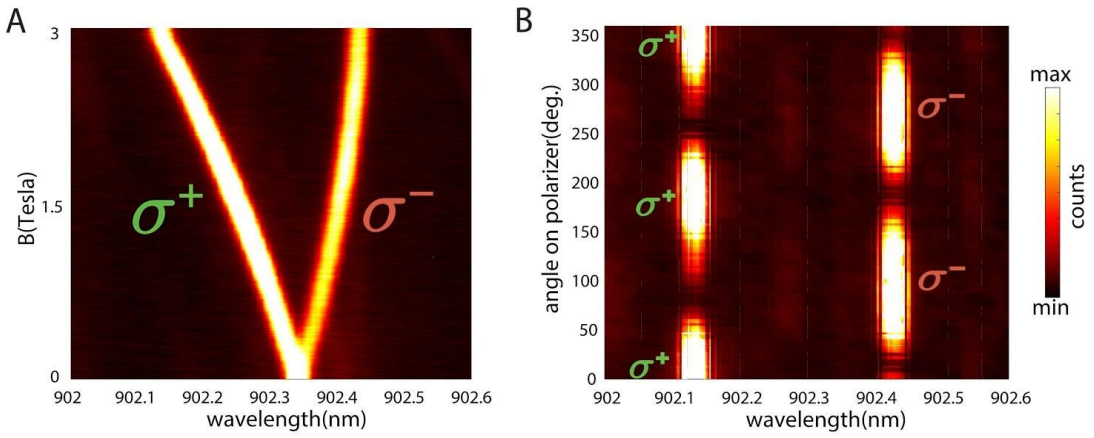

Figure S5. Polarization of quantum dot emission in bulk under magnetic field. (**A**) Splitting of single QD emission into σ+ and σ− exciton branches under application of magnetic field. (**B**) Verification of circular polarization of excitonic branches with polarization selective photoluminescence.

Coupling Efficiency

The coupling efficiency of emission from a single quantum emitter into the topological waveguide is defined by $\beta = \frac{I_L + I_R}{I_L + I_R + I_M}$ where I_L and I_R are the integrated photon counts propagating to the left and right waveguide modes respectively, and I_M is the photon counts emitted directly from the middle of the device into free space. We can estimate these intensities by measuring the brightness at the three locations denoted in the main text. Table S1 shows the coupling efficiencies calculated for different dots coupled to our topological device. The table reports integrated count rates for an integration time of 1s at each point. We determine the average to be 68%. If we take the estimated propagation loss into account (from Fig S3.B), the coupling efficiency will be higher at ~75%.

Coupled QDs	I_M	I_L	I_R	(%)
1	699	772	740	77.98
2	655	755	735	88.89
3	680	780	780	84.93
4	1300	1400	1900	75.23
5	802	1080	933	81.17
6	739	1021	654	78.85
7	795	1206	645	77.95
8	1090	1061	724	53.50
9	976	934	667	50.00
10	677	1079	807	92.44
11	869	728	819	54.90
12	1531	809	986	37.56
13	884	716	700	39.06
			Avg	68.65

Table S1. Estimation of coupling efficiency.

References and Notes

1. J. Dalibard, F. Gerbier, G. Juzeliūnas, P. Öhberg, Colloquium: Artificial gauge potentials for neutral atoms. *Rev. Mod. Phys.* **83**, 1523–1543 (2011). doi:10.1103/RevModPhys.83.1523

2. C. Eckardt, Atomic quantum gases in periodically driven optical lattices. *Rev. Mod. Phys.* **89**, 011004 (2017). doi:10.1103/RevModPhys.89.011004

3. M. Hafezi, J. M. Taylor, Topological physics with light. *Phys. Today* **67**, 68–69 (2014). doi:10.1063/PT.3.2394

4. L. Lu, J. D. Joannopoulos, M. Soljačić, Topological photonics. *Nat. Photonics* **8**, 821–829 (2014). doi:10.1038/nphoton.2014.248

5. L. Kane, T. C. Lubensky, Topological boundary modes in isostatic lattices. *Nat. Phys.* **10**, 39–45 (2014). doi:10.1038/nphys2835

6. J. Paulose, B. G. G. Chen, V. Vitelli, Topological modes bound to dislocations in mechanical metamaterials. *Nat. Phys.* **11**, 153–156 (2015). doi:10.1038/nphys3185

7. R. Süsstrunk, S. D. Huber, Observation of phononic helical edge states in a mechanical topological insulator. *Science* **349**, 47–50 (2015). doi:10.1126/science.aab0239 Medline

8. Z. Wang, Y. Chong, J. D. Joannopoulos, M. Soljacić, Observation of unidirectional backscattering-immune topological electromagnetic states. *Nature* **461**, 772–775 (2009). doi:10.1038/nature08293 Medline

9. X. Cheng, C. Jouvaud, X. Ni, S. H. Mousavi, A. Z. Genack, A. B. Khanikaev, Robust reconfigurable electromagnetic pathways within a photonic topological insulator. *Nat. Mater.* **15**, 542–548 (2016). doi:10.1038/nmat4573 Medline

10. M. Hafezi, S. Mittal, J. Fan, A. Migdall, J. M. Taylor, Imaging topological edge states in silicon photonics. *Nat. Photonics* **7**, 1001–1005 (2013). doi:10.1038/nphoton.2013.274

11. M. C. Rechtsman, J. M. Zeuner, Y. Plotnik, Y. Lumer, D. Podolsky, F. Dreisow, S. Nolte, M. Segev, A. Szameit, Photonic Floquet topological insulators. *Nature* **496**, 196–200 (2013). doi:10.1038/nature12066 Medline

12. M. Hafezi, E. A. Demler, M. D. Lukin, J. M. Taylor, Robust optical delay lines with topological protection. *Nat. Phys.* **7**, 907–912 (2011). doi:10.1038/nphys2063

13. L. Pilozzi, C. Conti, Topological lasing in resonant photonic structures. *Phys. Rev. B* **93**, 195317 (2016). doi:10.1103/PhysRevB.93.195317

14. G. Harari, M. A. Bandres, Y. Lumer, Y. Plotnik, D. N. Christodoulides, M. Segev, "Topological lasers," in *Conference on Lasers and Electro-Optics* [OSA Technical Digest (online), Optical Society of America, 2016], FM3A.3.

15. P. St-Jean, V. Goblot, E. Galopin, A. Lemaître, T. Ozawa, L. Le Gratiet, I. Sagnes, J. Bloch, A. Amo, Lasing in topological edge states of a one-dimensional lattice. *Nat. Photonics* **11**, 651–656 (2017). doi:10.1038/s41566-017-0006-2

16. P. Lodahl, S. Mahmoodian, S. Stobbe, A. Rauschenbeutel, P. Schneeweiss, J. Volz, H. Pichler, P. Zoller, Chiral quantum optics. *Nature* **541**, 473–480 (2017). doi:10.1038/nature21037 Medline

17. I. Carusotto, C. Ciuti, Quantum fluids of light. *Rev. Mod. Phys.* **85**, 299–366 (2013). doi:10.1103/RevModPhys.85.299

18. J. I. Cirac, H. J. Kimble, Quantum optics, what next? *Nat. Photonics* **11**, 18–20 (2017). doi:10.1038/nphoton.2016.259

19. D. G. Angelakis, Ed., *Quantum Simulations with Photons and Polaritons* (Springer International Publishing, 2017).

20. L. H. Wu, X. Hu, Scheme for achieving a topological photonic crystal by using dielectric material. *Phys. Rev. Lett.* **114**, 223901 (2015). doi:10.1103/PhysRevLett.114.223901 Medline

21. S. Barik, H. Miyake, W. DeGottardi, E. Waks, M. Hafezi, Two-dimensionally confined topological edge states in photonic crystal. *New J. Phys.* **18**, 113013 (2016). doi:10.1088/1367-2630/18/11/113013

22. Materials and methods are available as supplementary materials.

23. M. Bayer, G. Ortner, O. Stern, A. Kuther, A. A. Gorbunov, A. Forchel, P. Hawrylak, S. Fafard, K. Hinzer, T. L. Reinecke, S. N. Walck, J. P. Reithmaier, F. Klopf, F. Schäfer, Fine structure of neutral and charged excitons in self-assembled In(Ga)As/(Al)GaAs quantum dots. *Phys. Rev. B* **65**, 195315 (2002). doi:10.1103/PhysRevB.65.195315

24. J. Petersen, J. Volz, A. Rauschenbeutel, Chiral nanophotonic waveguide interface based on spin-orbit interaction of light. *Science* **346**, 67–71 (2014). doi:10.1126/science.1257671 Medline

25. I. Söllner, S. Mahmoodian, S. L. Hansen, L. Midolo, A. Javadi, G. Kiršanskė, T. Pregnolato, H. El-Ella, E. H. Lee, J. D. Song, S. Stobbe, P. Lodahl, Deterministic photon-emitter coupling in chiral photonic circuits. *Nat. Nanotechnol.* **10**, 775–778 (2015). doi:10.1038/nnano.2015.159 Medline

26. T. Kariyado, X. Hu, Topological states characterized by mirror winding numbers in graphene with bond modulation. *Sci. Rep.* **7**, 16515 (2017). doi:10.1038/s41598-017-16334-0 Medline

27. H. Pichler, T. Ramos, A. J. Daley, P. Zoller, Quantum optics of chiral spin networks. *Phys. Rev. A* **91**, 042116 (2014). doi:10.1103/PhysRevA.91.042116

28. M. Ringel, M. Pletyukhov, V. Gritsev, Topologically protected strongly correlated states of photons. *New J. Phys.* **16**, 113030 (2014). doi:10.1088/1367-2630/16/11/113030

29. A. Metelmann, A. A. Clerk, Nonreciprocal photon transmission and amplification via reservoir engineering. *Phys. Rev. X* **5**, 021025 (2015). doi:10.1103/PhysRevX.5.021025

30. R. O. Umucalılar, I. Carusotto, Fractional quantum Hall states of photons in an array of dissipative coupled cavities. *Phys. Rev. Lett.* **108**, 206809 (2012). doi:10.1103/PhysRevLett.108.206809 Medline

31. M. Hafezi, M. D. Lukin, J. M. Taylor, Non-equilibrium fractional quantum Hall state of light. *New J. Phys.* **15**, 063001 (2013). doi:10.1088/1367-2630/15/6/063001